MTLA 33 (2024) 102020

Contents lists available at ScienceDirect

Materialia

journal homepage: www.elsevier.com/locate/mtla

On the superelastic behavior during spherical nanoindentation of a Ni-Ti shape memory alloy

Hang Li [a], Zhe Gao [b], Jin-Yoo Suh [c], Heung Nam Han [d], Upadrasta Ramamurty [e,f], Jae-il Jang [b,*]

[a] College of Materials Science and Engineering, Heilongjiang University of Science and Technology, Harbin 150027, China
[b] Division of Materials Science and Engineering, Hanyang University, Seoul 04763, South Korea
[c] Center for Energy Materials Research, Korea Institute of Science and Technology, Seoul 02792, South Korea
[d] Department of Materials Science and Engineering and Research Institute of Advanced Materials, Seoul National University, Seoul 08826, South Korea
[e] School of Mechanical and Aerospace Engineering, Nanyang Technological University, Singapore 639798, Singapore
[f] Institute of Materials Research Engineering, Agency for Science, Technology and Research, Singapore 138634, Singapore

ARTICLE INFO

Keywords:
Nanoindentation
Shape memory alloys
Superelasticity
NiTi

ABSTRACT

Nanoindentation, the most widely-used probe for small-scall mechanical property evaluation, has been increasingly adopted for exploring the local behavior of shape memory alloys (SMAs). Herein, we explore the influence of the testing parameters (i.e., peak load, indenter radius, loading/unloading rate, and cyclic loading) on the superelastic behavior of a Ni-Ti SMA at room temperature, at which it is in the austenitic state, during spherical nanoindentation. The possible underlying mechanisms for measured response due to each of the testing parameters are discussed in terms of the roles of forward/reverse stress-induced phase transformations, dislocation activity, latent heat evolution, and geometric compatibility of the interfaces during the post-yield deformation.

Since the discovery that the equiatomic NiTi exhibits fully reversible stress-induced phase transformation, shape memory alloys (SMAs) have attracted considerable attention, both from the scientific and technological perspectives. They now find applications in automotive, aerospace, biomedical, and robotics industries [1–4]. In most cases, the sizes of the SMA components or devices are generally small (and likely to get smaller in future), which makes precise measurement of their 'small volume' properties and their local variations in SMAs more technologically relevant. Nanoindentation technique is apt for probing this. Consequently, the superelastic (SE) (or pseudoelastic) characteristics of SMAs has been widely investigated using room-temperature nanoindentation experiments. Variations in properties including energy dissipation [5–8], microstructure [9,10], hardness impression [11–14], indentation depth [15–22], and constitutive relation [23–26] were explored. In this context, it is important to note that the results from nanoindentation experiments are often sensitive to the testing conditions. Their influence on the result is generally NOT an experimental artifact, but mostly caused by intrinsic nature of the material being probed. Therefore, a systematic and thorough investigation into such effects is essential for obtaining the data appropriate for the purpose of the design. Keeping this in view, here we systematically examined examine the influence of various indentation variables (peak load, indenter radius, loading/unloading rate, and cyclic loading) on the small-scale superelastic behavior of a NiTi SMA (one of the most popularly used SMAs) through a series of spherical nanoindentation experiments, and the revealed results are discussed in terms of the governing deformation mechanisms.

The SMA sample utilized here is a Ni-49.1Ti (at%) solid-solution alloy (having average grain size of ~ 60 μm, as shown in Fig. S1 of Supplementary Material) that was solution treated at 950 °C for 2 h and then water quenched. X-ray diffraction (XRD; Rigaku, Ultima IV) pattern obtained at 18 °C (see inset of Fig. 1a) confirms B2 structure austenite, implying austenite finish temperature, A_f, is below 18 °C and thus SE can be observed at room temperature (~ 25 °C). The austenite state of the alloy is further confirmed using differential scanning calorimetry (DSC; TA, DSC2010). Results displayed in Fig. 1a show only a pair of endothermic and exothermic peaks, indicating that the alloy has a one-step phase transition of B2-B19' [27].

Nanoindentation experiments were performed using the Nanoindenter-XP (KLA) instrument with three different spherical indenters with tip radii, *R*, of 1.84, 11.51, and 34.94 μm (determined by Hertzian contact analysis of indentations made on fused quartz

* Corresponding author.
E-mail address: jijang@hanyang.ac.kr (J.-i. Jang).

https://doi.org/10.1016/j.mtla.2024.102020
Received 14 January 2024; Accepted 21 January 2024
Available online 22 January 2024

samples). All the probed surfaces were vibration-polished beforehand with 0.02 μm colloidal silica. More than 10 indentations were conducted for each condition. The microstructures of the region underneath the indenter were examined using transmission electron microscopy (TEM; FEI Co., Tecnai F20). Focused ion beam (FIB; FEI Co., Nova 200 NanoLab) milling was performed to obtain TEM specimen at the vertical cross-sections of the deformed regions right underneath the indenter.

Fig. 1b shows the representative indentation load-displacement (P–h) curves (for R = 11.51 and 1.84 μm) obtained at different peak loads, P_{max}. The reproducibility of the indentation results is attested by the overlap of the loading curves obtained with different P_{max}. The inset confirms that even the indentation response obtained with the lowest P_{max} (10 mN) is not fully elastic. In the nanoindentation tests of SMAs, the ratio of depth recovery after unloading (i.e., $(h_{max} - h_f)/h_{max}$ where h_{max} and h_f are the maximum and final displacements, respectively) is often taken as a proxy indicator for SE [15,18,19,20,26]. Note that to account for the slight h change, which occurs due to the thermal drift during the correction process at $0.1P_{max}$, h_f was determined by fitting the early 90 % part of unloading curve (i.e., unloading part shown in Fig. 1b) with P vs. h^2 relation.

Deformation underneath the indenter: Typical uniaxial loading-unloading stress-strain response of the NiTi SMA at a temperature above A_f is schematically illustrated in Fig. 2a where governing mechanisms for each sequence are also mentioned. Note that dislocation slip in austenite can occur during stress-induced martensitic transformation (SIMT) of some NiTi SMAs (e.g., nanocrystalline or ultrafine-grained NiTi wire samples [28]). For the examined SMA in this study, however, the critical stress for SIMT is less than the yield stress of austenite, and plastic deformation of austenite cannot precede SIMT [29–31]. Upon loading, post-yield deformation is governed by two independent mechanisms [32–34]: (a) SIMT from B2 to B19' and (b) dislocation glide within the stress-induced martensite (SIM). Unlike the latter, the former can be almost completely recovered by the reverse transformation after removing the applied stress. Initial elastic deformation is followed by straining via SIMT (often observed as a plateau in stress-strain curve). Then, at the end of the plateau, dislocation slip occurs in SIM, which, in turn, stabilizes it by hindering the reverse motion of the interfaces during unloading. In the first stage of the unloading curve, the strain recovery occurs due to the reorientation and elastic recovery of SIM. In the following plateau stage, the strain recovery is mainly caused by the reverse transformation from SIM to austenite. Then, at the end of the plateau, the elastic recovery of austenite begins.

During indentation, a steep spatial variation in the stress and strain distributions underneath the indenter can exist [35,36]. Therefore, the mechanisms described in Fig. 2a can be in operation simultaneously at different locations. The most likely microstructure underneath a spherical indenter is schematically illustrated in Fig. 2b. It was arrived at on the basis of mechanisms suggested in literature, for the widely-reported microstructure of tensile-deformed SMAs (phase transformation dislocations, PTDs [26], statistically stored dislocations, SSDs [26], and SIMs [37]) combined with that for the general distribution of geometrically necessary dislocations (GNDs) distribution underneath a spherical indenter [38]. Note that the orientations of residual SIMs are random and do not strictly correspond to the distribution of dislocations [37,39]. Such microstructural evolution is partly confirmed the representative TEM image (Fig. 2c) obtained from the deformed region underneath the indenter, directly demonstrating the distribution of dislocations and the morphology of residual SIMs. In the highly stressed region right below the indenter, dislocation density is the highest with simultaneous existence of the lath-like residual SIMs.

As illustrated in Fig. 2b, the governing mechanism can be categorized into three groups, depending on the applied stress level. In the regions of relatively low stresses, the following three different deformation mechanisms can operate simultaneously: elastic deformation of austenite, SIMT, and elastic deformation and/or reorientation of SIM. When SIMT occurs, it was observed experimentally that PTDs are generated during the movement of the austenite-martensite interfaces due to the poor geometric compatibility at the developing interface [40–42]. They can resist the reverse motion of the interfaces during unloading, resulting in residual SIM.

Based on the above scenario, it is possible that, in the relatively low stress regions, the inelastic strains caused by PTDs (and thus residual SIM) are unrecoverable, whereas the strains caused by the deformation of austenite and SIM are fully recovered. In the regions of higher stresses, a larger proportion of austenite would have undergone SIMT. At the same time, glide of SSDs could occur in some SIMs. In the most highly stressed regions, there should be only SIM and plasticity through dislocation glide occurs within it. Furthermore, since such regions are right below the indenter, GNDs are the most actively generated, which also impede the reverse transformation (as PTDs do) and result in residual SIM. As expected, dislocation glide within SIMs is a crucial source of nonrecoverable strain remaining after unloading.

Effect of indentation load Unlike the indentation with a sharp tip (such as Vickers), that performed with a spherical indenter is not geometrically self-similar, i.e., for a given R, the stress distribution underneath it evolves with increasing P. A possible way to obtain geometrically similar indentation is using indenters with different R. If the indentation strain, ε_i (given by $\varepsilon_i = 0.2(a_c/R)$ where a_c is the contact radius [43,44]) is maintained constant, the mean contact pressure (i.e., hardness) may be constant and the indentations are geometrically similar [45]. Thus, the nanoindentation results obtained with indenters of different radii can be directly compared at the same ε_i instead of the same P_{max} or h_{max}. Fig. 3 summarizes the variations in recovery ratio (at given loading rates marked in the figure) as a function of ε_i achieved at

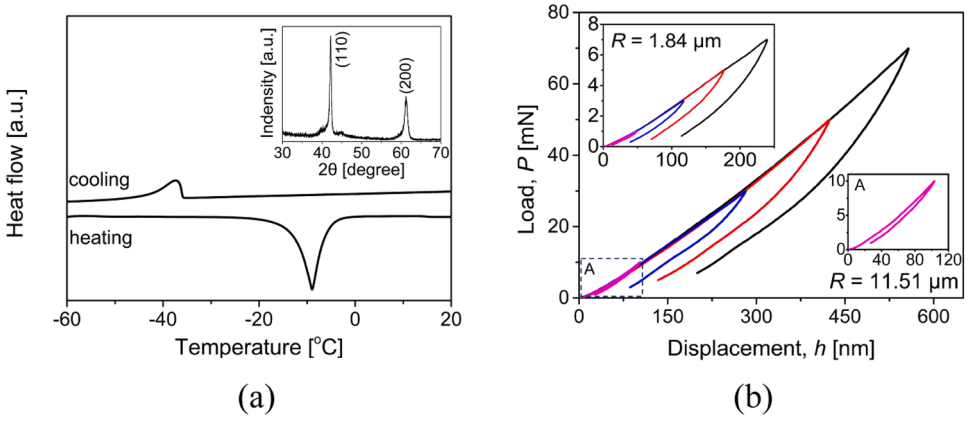

Fig. 1. (a) DSC curves of solution-treated Ni-49.1Ti alloy (with inset showing XRD pattern), and (b) representative P–h curves obtained at different P_{max} (for R = 1.84 and 11.51 μm).

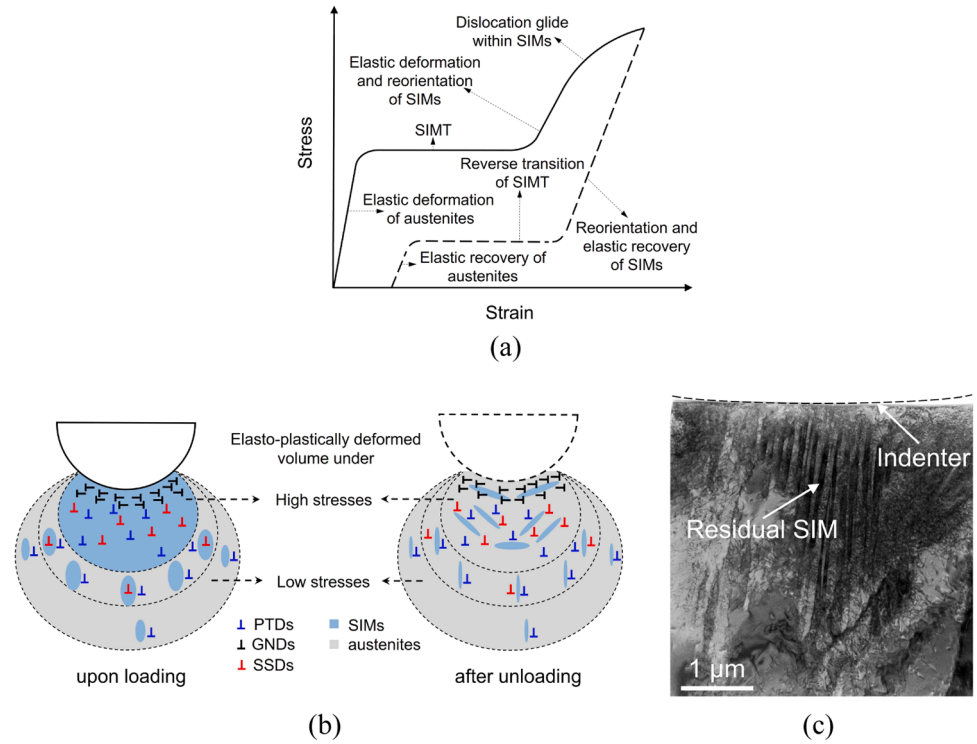

Fig. 2. Schematic diagrams of (a) deformation mechanisms in uniaxial tension and (b) structural change during spherical indentation (SIMs: stress-induced martensites; PTDs: phase transformation dislocations; GNDs: geometrically necessary dislocations; SSDs: statistically stored dislocations). (c) Representative TEM image showing the deformed microstructure underneath the indenter (for R = 11.51 μm, P_{max} = 70 mN, dP/dt = 8 mN/s).

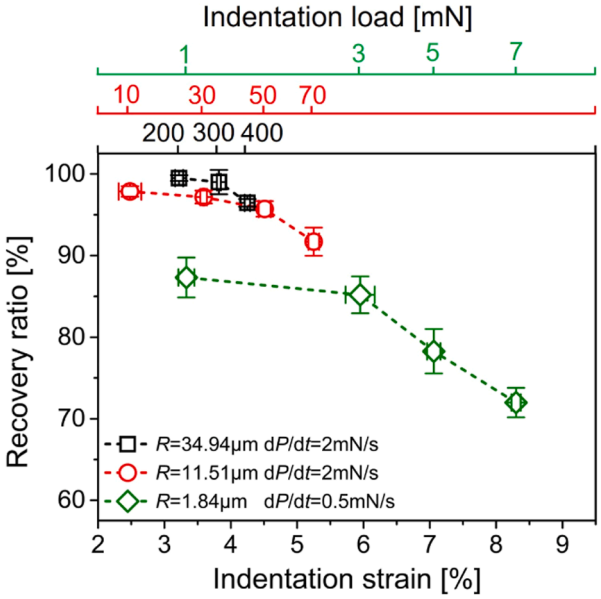

Fig. 3. Recovery ratio as a function of the indentation load and strain for different indenter radii.

various P_{max}. In the figure, only three datasets are provided for R = 34.94 μm because the recovery ratios for 200 and 300 mN already reached almost 100 %, while the loading and unloading curves obtained at a lower load (e.g., 100 mN) are too close to each other making it difficult to estimate recovery ratio in an accurate manner. Two features are evident in Fig. 3. First, for all three R, the recovery ratio is reduced with increasing P_{max} and ε_i. Second, at a given ε_i, the recovery ratio is more pronounced for a larger R.

The observed reduction in recovery ratio with increasing P_{max} and ε_i for a given R, is in agreement with the literature data [15,19,26]. It can be explained in consideration of tensile behavior in Fig. 2a. Although there might be severe stress and strain gradients underneath the indenter, each point experiences independently a series of different deformation mechanisms following the manner described in Fig. 2a; i.e., elastic deformation of pristine austenite, SIMT, and dislocation glide within SIMs. As P_{max} increases, (1) at a given point, the probability of nonrecoverable deformation increases and (2) the nonrecoverably-deformed volume becomes enlarged, which results in a decrease in the recovery ratio.

Effect of indenter radius As shown in Fig. 3, the recovery ratio for a larger R at a given ε_i is higher than that for a smaller R, which is consistent with the previous report by Kumar *et al.* [26]. This new case of size effect can be understood in a similar manner to that used for explaining indentation size effect (ISE) during spherical indentation [46,47]. In the ISE theory, the average density of GNDs is inversely proportional to R; for a smaller R, the density is larger. As mentioned earlier, in SMAs, different kinds of dislocations including PTDs, SSDs, and GNDs impede the reverse transformation that results in some residual SIM upon unloading. Therefore, smaller density of GNDs underneath a larger indenter may lead to a smaller amount of residual SIM, resulting in a higher recovery ratio. It is noteworthy that the R effect is exponentially decaying with R value, implying the ISE is much clearer for small R [46,47]. A good example can be found in Ref. [15] where for two large R (213.4 and 106.7 μm), there is an insignificant difference in the recovery ratio at a given ε_i, although the reason behind was not provided in that paper.

Effect of indentation rate The recovery ratios for two different R (1.84 and 11.51 μm) as a function of the loading and unloading rate are summarized in Fig. 4. Since the adopted P_{max} was 3 and 50 mN (corresponding to ε_i of ~ 6 and 5 %, respectively) for R of 1.84 and 11.51 μm, respectively, the examined range of the rates were quite different for two R. It is evident in Fig. 4 that as the loading rate decreases, the

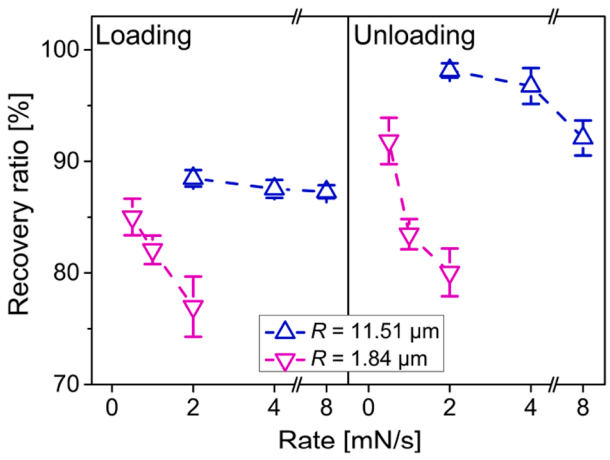

Fig. 4. Recovery ratios as a function of loading and unloading rate for two different indenter radii (R = 1.84 and 11.51 μm).

recovery ratio increases. In addition, a comparison of the TEM images obtained from the deformed regions (made with for two different rates, Figs. 2c and S2 for the loading/unloading rates of 8 and 2 mN/s, respectively) reveals that with reducing the rates, the dislocation density decreases significantly, and there is no residual SIMs. This result may be explained as follows.

Effect of loading rate: A higher loading rate has an effect on SIMT from the kinetics point of view. Not enough time is allowed for the stabilization of the interfaces between the two phases. As a result, and due to sub-optimized growth orientation of SIM within the parent austenite phase, the dislocation density within them will be higher [48]. This enhanced dislocation activity during SIMT may lead to a lower recovery ratio.

Effect of unloading rate: The latent heat stored in the stressed volume plays a significant role in the reverse transformation from SIM to austenite upon unloading. The reverse transformation is an endothermic process; the interface retreats and the transformed volume returns to austenitic phase by absorbing the latent heat [27]. Since heat conduction is a highly rate-dependent kinetic phenomenon in the unloading stage [8], an increase in unloading rate leads to insufficient supply of heat required for the reverse transformation, which, in turn, results in increased amount of residual SIM and thus a reduced recovery ratio.

Effect of cyclic loading Fig. 5a shows the representative P–h curves (for R = 11.51 μm) recorded during cyclic indentations where P_{max} and loading/unloading rate were fixed as 30 mN (corresponding to ε_i of ~ 3.6 %) and 2 mN/s, respectively. For clarity, the inset of Fig. 5a exhibits each indentation cycle separately. As seen, a large hysteresis loop forms in the first cycle, but the loops degenerate in the following cycles. The variation of the dissipated energy, determined from the area of the loop in each cycle, with the number of cycles is shown in Fig. 5b. It is evident that during the early cycles, the dissipated energy decreases dramatically, e.g., the dissipated energy (~ 0.33 nJ) of the second cycle is much lower than that (~ 0.53 nJ) of the first cycle. Then, the decreasing trend gradually slows down. This behavior is similar to the results from superelastic cycling tests under uniaxial tension [30].

During cyclic indentations, SIM undergoes repeated reorientation to achieve the most favorable orientation for nucleation and growth from the austenitic phase [49,50]. This process gradually improves the geometrical compatibility at the interface between the martensite and austenite; a good compatibility significantly reduces the internal friction (which the dissipated energy is mainly used to overcome), caused by the back-and-forth movement of the interface during the phase transformation [35,51,52]. Note that differentiating cyclic work hardening from SMA characteristics is very difficult, since no matter how cyclic deformation happens in a SMA, cyclic work hardening occurs upon the process [30,53]. The key dislocation activity during cyclic loading in the present context is the generation of PTDs. As the cycle number increases, more PTDs are generated, but their generation rate gradually decreases due to the improvement of the geometric compatibility and cyclic work hardening. As a result, the dissipation energy related to the enhanced dislocation activity shows a similar increasing trend, but is much smaller than the decrease in dissipation energy caused by the former (improved interfacial compatibility). Subsequently, both the improvement in the compatibility and the increase in PTDs reach saturation, resulting in the observed trend of the dissipation energy.

In summary, here a parametric evaluation of the small-scale superelastic behavior of a NiTi SMAs via spherical nanoindentation is conducted, in terms of controllable indentation parameters. As the experimental results show, the peak load, indenter radius, loading/unloading rate, and cyclic loading affect the measured response in different ways. The observed trends can be rationalized by recourse to the roles of forward and reverse SIMT, dislocation activities, absorption of latent heat, and geometric compatibility between two phases (martensite and austenite) in the post-yield deformation. Based on the indentation parameters examined, appropriate testing condition for a proper characterization of the superelasticity and its effect in SMAs utilizing nanoindentation can be identified. For instance, for examining the maximum extent of superelasticity, it is necessary to utilize an indenter having a large radius (to reduce the amount of GNDs) and very low loading- and unloading-rates (to weaken the dislocation activities

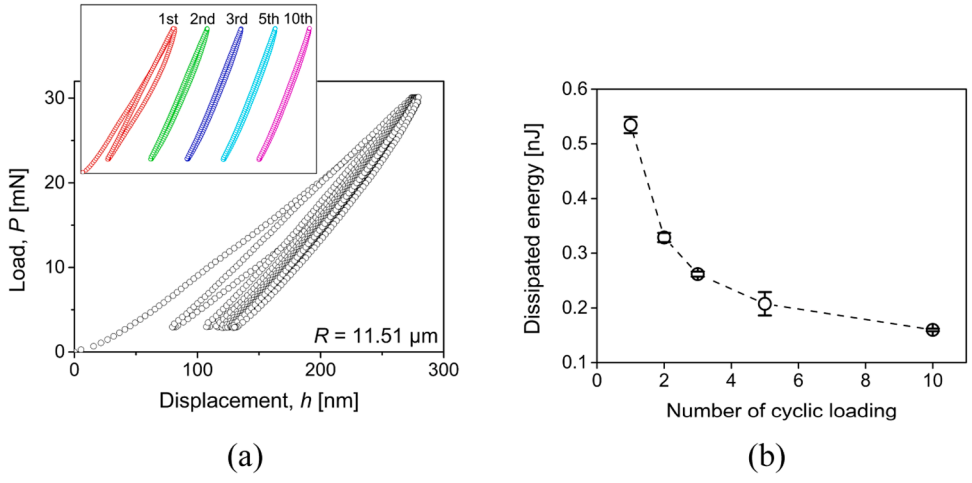

Fig. 5. Results from cyclic indentation tests; (a) representative P–h curves (with inset showing the unloading-reloading cycle separately for clarity) and (b) the dissipated energy as a function of the number of cyclic loading.

during SIMT and supply sufficient heat for the reverse transformation). Although not covered in the present paper, a precise estimation of global stress-strain relation (especially the unloading part) using spherical indentation (following the limited previous works [23–26]) deserves attention in future research considering its significance for linking local microscopic property to global macroscopic performance in SMAs.

Declaration of competing interest

The authors declare that they have no known competing financial interests or personal relationships that could have appeared to influence the work reported in this paper.

Acknowledgements

The work at Heilongjiang University of Science and Technology was supported in part by the Fundamental Research Funds for Universities of Heilongjiang Province (No. 2020-KYYWF-0683), and in part by the China Scholarship Council Visiting Scholar Program (No. 201908230066). The work at Hanyang University was supported by the National Research Foundation of Korea (NRF) grants funded by the Korea government (MSIT) (No. 2022R1A5A1030054 and RS-2023–00273384). The work at Nanyang Technological University was supported by the Agency for Science, Technology and Research (A*STAR) of Singapore via the Structural Metal Alloys Programme (No. A18B1b0061).

Supplementary materials

Supplementary material associated with this article can be found, in the online version, at doi:10.1016/j.mtla.2024.102020.

References

[1] J.M. Jani, M. Leary, A. Subic, M.A. Gibson, A review of shape memory alloy research, applications and opportunities, Mater. Design 56 (2014) 1078–1113, https://doi.org/10.1016/j.matdes.2013.11.084.
[2] K. Yamauchi, I. Ohkata, K. Tsuchiya, S. Miyazaki, Shape Memory and Superelastic alloys: Applications and Technologies, Elsevier, 2011. https://www.sciencedirect.com/book/9781845697075/shape-memory-and-superelastic-alloys.
[3] D.C. Lagoudas, Shape memory alloys, Science and Business Media (2008), https://doi.org/10.1007/978-0-387-47685-8. LLC.
[4] D.J. Hartl, D.C. Lagoudas, Aerospace applications of shape memory alloys, Proc. Inst. Mech. Eng. Part G J. Aerosp. Eng. 221 (2007) 535–552, https://doi.org/10.1243/09544100JAERO211.
[5] K. Gall, K. Jumtunen, H.J. Maier, H. Sehitoglu, Y.I. Chumlyakov, Instrumented micro-indentation of NiTi shape-memory alloys, Acta Mater. 49 (2001) 3205–3217, https://doi.org/10.1016/S1359-6454(01)00223-3.
[6] X.G. Ma, K. Komvopoulos, Pseudoelasticity of shape-memory titanium–nickel films subjected to dynamic nanoindentation, Appl. Phys. Lett. 84 (2004) 4274, https://doi.org/10.1063/1.1737463.
[7] M. Arciniegas, Y. Gaillard, J. Peña, J.M. Manero, F.J. Gil, Thermoelastic phase transformation in TiNi alloys under cyclic instrumented indentation, Intermetallics 17 (2009) 784–791, https://doi.org/10.1016/j.intermet.2009.03.020.
[8] A. Amini, C. Cheng, A. Asgari, Combinational rate effects on the performance of nano-grained pseudoelastic Nitinols, Mater. Lett. 105 (2013) 98–101, https://doi.org/10.1016/j.matlet.2013.04.072.
[9] H.X. Zheng, J.C. Rao, J. Pfetzing, J. Frenzel, C. Somsen, G. Eggeler, TEM observation of stress-induced martensite after nanoindentation of pseudoelastic $Ti_{50}Ni_{48}Fe_2$, Scripta Mater. 58 (2008) 743–746, https://doi.org/10.1016/j.scriptamat.2007.12.012.
[10] J. Pfetzing-Micklich, C. Somsen, A. Dlouhy, C. Begau, A. Hartmaier, M.F. X. Wagner, G. Eggeler, On the crystallographic anisotropy of nanoindentation in pseudoelastic NiTi, Acta Mater. 61 (2013) 602–616, https://doi.org/10.1016/j.actamat.2012.09.081.
[11] C.P. Frick, T.W. Lang, K. Spark, K. Gall, Stress-induced martensitic transformations and shape memory at nanometer scales, Acta Mater. 54 (2006) 2223–2234, https://doi.org/10.1016/j.actamat.2006.01.030.
[12] G. Laplanche, J. Pfetzing-Micklich, G. Eggeler, Orientation dependence of stress-induced martensite formation during nanoindentation in NiTi shape memory alloys, Acta Mater. 68 (2014) 19–31, https://doi.org/10.1016/j.actamat.2014.01.006.
[13] G. Laplanche, J. Pfetzing-Micklich, G. Eggeler, Sudden stress-induced transformation events during nanoindentation of NiTi shape memory alloys, Acta Mater. 78 (2014) 144–160, https://doi.org/10.1016/j.actamat.2014.05.061.
[14] V.V. Shastry, V.D. Divya, M.A. Azeem, A. Paul, D. Dye, U. Ramamurty, Combining indentation and diffusion couple techniques for combinatorial discovery of high temperature shape memory alloys, Acta Mater. 61 (2013) 5735–5742, https://doi.org/10.1016/j.actamat.2013.06.017.
[15] W.Y. Ni, Y.T. Cheng, D.S. Grummon, Microscopic shape memory and superelastic effects under complex loading conditions, Surf. Coat. Tech. 177-178 (2004) 512–517, https://doi.org/10.1016/S0257-8972(03)00920-4.
[16] A.J.M. Wood, T.W. Clyne, Measurement and modelling of the nanoindentation response of shape memory alloys, Acta Mater. 54 (2006) 5607–5615, https://doi.org/10.1016/j.actamat.2006.08.013.
[17] A. Amini, Y. He, Q. Sun, Loading rate dependency of maximum nanoindentation depth in nano-grained NiTi shape memory alloy, Mater. Lett. 65 (2011) 464–466, https://doi.org/10.1016/j.matlet.2010.10.026.
[18] V.V. Shastry, U. Ramamurty, Temperature dependence of indentation recovery ratios in austenitic and martensitic shape memory alloys, Smart Mater. Struct. 22 (2013) 077002, https://doi.org/10.1088/0964-1726/22/7/077002.
[19] C.H. Chen, S.Y. Cheng, S.K. Wu, Nanoindentation studies on precipitation hardening of Ti-rich $Ti_{50.4}Ni_{49.5}Si_{0.1}$ shape memory ribbons, Intermetallics 36 (2013) 109–117, https://doi.org/10.1016/j.intermet.2013.01.009.
[20] V.V. Shastry, U. Ramamurty, Simultaneous measurement of mechanical and electrical contact resistances during nanoindentation of NiTi shape memory alloys, Acta Mater. 61 (2013) 5119–5129, https://doi.org/10.1016/j.actamat.2013.04.049.
[21] J. Anuja, R. Narasimhan, U. Ramamurty, A numerical study of the indentation mechanics of shape memory alloys in different temperature regimes, Mech. Mater. 139 (2019) 103212, https://doi.org/10.1016/j.mechmat.2019.103212.
[22] J. Anuja, R. Narasimhan, U. Ramamurty, Effects of superelasticity and plasticity on the spherical indentation response of shape memory alloys a finite element analysis, Smart Mater. Struct. 28 (2019) 035028, https://doi.org/10.1088/1361-665X/aaff88.
[23] H.S. Zhang, K. Komvopoulos, Nanoscale Pseudoelasticity of Single-crystal Cu–Al–Ni shape-memory Alloy Induced by Cyclic Nanoindentation, J. Mater. Sci. 41 (2006) 5021–5024, https://doi.org/10.1007/s10853-006-0124-6.
[24] L. Qian, S. Zhang, D. Li, Z. Zhou, Spherical indentation for determining the phase transition properties of shape memory alloys, J. Mater. Res. 24 (2009) 1082, https://doi.org/10.1557/JMR.2009.0082.
[25] G. Pan, Z. Cao, M. Wei, L. Xu, J. Shi, X. Meng, Superelasticity of TiNi thin films induced by cyclic nanoindentation deformation at nanoscale, Mat. Sci. Eng. A 600 (2014) 8–11, https://doi.org/10.1016/j.msea.2014.02.019.
[26] S. Kumar, I.A. Kumar, L. Marandi, I. Sen, Assessment of small-scale deformation characteristics and stress-strain behavior of NiTi based shape memory alloy using nanoindentation, Acta Mater. 201 (2020) 303–315, https://doi.org/10.1016/j.actamat.2020.09.080.
[27] S. Sarkar, X.B. Ren, K. Otsuka, Evidence for Strain Glass in the Ferroelastic-Martensitic System $Ti_{50-x}Ni_{50+x}$, Phys. Rev. Lett. 95 (2005) 205702, https://doi.org/10.1103/PhysRevLett.95.205702.
[28] R. Delville, B. Malard, J. Pilch, P. Sittner, D. Schryvers, Transmission electron microscopy investigation of dislocation slip during superelastic cycling of Ni–Ti wires, Int. J. Plasticity 27 (2011) 282–297, https://doi.org/10.1016/j.ijplas.2010.05.005.
[29] S. Miyazaki, T. Imai, K. Otsuka, Y. Suzuki, Lüders-like Deformation Observed in the Transformation Pseudoelasticity of a Ti-Ni Alloy, Scripta Metal. 15 (1981) 853–856, https://doi.org/10.1016/0036-9748(81)90265-9.
[30] S. Miyazaki, T. Imai, Y. Igo, K. Otsuka, Effect of cyclic deformation on the pseudoelasticity characteristics of Ti-Ni alloys, Metall. Trans. A 17A (1986) 115–120, https://doi.org/10.1007/BF02644447.
[31] X. Huang, Y. Liu, Effect of annealing on the transformation behavior and superelasticity of NiTi shape memory alloy, Scripta Mater. 45 (2001) 153–160, https://doi.org/10.1016/S1359-6462(01)01005-3.
[32] S. Miyazaki, K. Otsuka, Y. Suzuki, Transformation pseudoelasticity and deformation behavior in a Ti-50.6 at% Ni alloy, Scripta Metall. 15 (1981) 287–292, https://doi.org/10.1016/0036-9748(81)90346-X.
[33] J.A. Shaw, S. Kyriakides, Thermomechanical aspects of NiTi, J. Mech. Phys. Solids 43 (1995) 1243–1281, https://doi.org/10.1016/0022-5096(95)00024-D.
[34] D.S. Ford, S.R. White, Thermomechanical behavior of 55Ni45Ti NITINOL, Acta Mater. 44 (1996) 2295–2307, https://doi.org/10.1016/1359-6454(95)00343-6.
[35] N.A. Fleck, Strain gradient plasticity, Adv. Appl. Mech. 33 (1997) 296–361.
[36] M.M. Chaudhri, Subsurface plastic strain distribution around spherical indentations in metals, Philos. Mag. A 74 (1996) 1213–1224, https://doi.org/10.1080/01418619608239721.
[37] P. Chowdhury, H. Sehitoglu, A revisit to atomistic rationale for slip in shape memory alloys, Prog. Mater Sci. 85 (2017) 1–42, https://doi.org/10.1016/j.pmatsci.2016.10.002.
[38] H.J. Gao, Y.G. Huang, Geometrically necessary dislocation and size-dependent plasticity, Scripta Mater. 48 (2003) 113–118, https://doi.org/10.1016/S1359-6462(02)00329-9.
[39] K.F. Xu, J. Luo, C. Li, Y.L. Shen, C.J. Li, X. Ma, M.Q. Li, Mechanisms of stress-induced martensitic transformation and transformation-induced plasticity in NiTi shape memory alloy related to superelastic stability, Scripta Mater. 217 (2022) 114775, https://doi.org/10.1016/j.scriptamat.2022.114775.
[40] R.F. Hamilton, H. Sehitoglu, Y. Chumlyakov, H.J. Maier, Stress dependence of the hysteresis in single crystal NiTi alloys, Acta Mater. 52 (2004) 3383–3402, https://doi.org/10.1016/j.actamat.2004.03.038.
[41] P. Sedmák, P. Šittner, J. Pilch, C. Curfs, Instability of cyclic superelastic deformation of NiTi investigated by synchrotron X-ray diffraction, Acta Mater. 94 (2015) 257–270, https://doi.org/10.1016/j.actamat.2015.04.039.

[42] R. Zarnetta, R. Takahashi, M.L. Young, A. Savan, Y. Furuya, S. Thienhaus, B. Maaß, M. Rahim, J. Frenzel, H. Brunken, Y.S. Chu, V. Srivastava, R.D. James, I. Takeuchi, G. Eggeler, A. Ludwig, Identification of quaternary shape memory alloys with near-zero thermal hysteresis and unprecedented functional stability, Adv. Funct. Mater. 20 (2010) 1917–1923, https://doi.org/10.1002/adfm.200902336.
[43] W.C. Oliver, G.M. Pharr, An improved technique for determining hardness and elastic modulus using load and displacement sensing indentation experiments, J. Mater. Res. 7 (1992) 1564–1583, https://doi.org/10.1557/JMR.1992.1564.
[44] W.C. Oliver, G.M. Pharr, Measurement of hardness and elastic modulus by instrumented indentation: Advances in understanding and refinements to methodology, J. Mater. Res. 19 (2004) 3–20, https://doi.org/10.1557/jmr.2004.19.1.3.
[45] A.C. Fischer-Cripps, Nanoindentation, third ed., Springer, New York, 2011 https://doi.org/10.1007/978-1-4419-9872-9.
[46] J.G. Swadener, E.P. George, G.M. Pharr, The correlation of the indentation size effect measured with indenters of various shapes, J. Mech. Phys. Solids 50 (2002) 681–694, https://doi.org/10.1016/S0022-5096(01)00103-X.
[47] G.M. Pharr, E.G. Herbert, Y.F. Gao, The indentation size effect: a critical examination of experimental observations and mechanistic interpretations, Annu. Rev. Mater. Res. 40 (2010) 271–292, https://doi.org/10.1146/annurev-matsci-070909-104456.
[48] R.J. Wasilewski, On the nature of the martensitic transformation, Metall. Trans. A 6 (1975) 1405–1418, https://doi.org/10.1007/BF02641933.
[49] B. Ye, B.S. Majumdar, I. Dutta, Texture development and strain hysteresis in a NiTi shape-memory alloy during thermal cycling under load, Acta Mater. 57 (2009) 2403–2417, https://doi.org/10.1016/j.actamat.2009.01.032.
[50] N.G. Jones, D. Dye, Martensite evolution in a NiTi shape memory alloy when thermal cycling under an applied load, Intermetallics 19 (2011) 1348–1358, https://doi.org/10.1016/j.intermet.2011.03.032.
[51] X.L. Meng, H. Li, W. Cai, S.J. Hao, L.S. Cui, Thermal cycling stability mechanism of $Ti_{50.5}Ni_{33.5}Cu_{11.5}Pd_{4.5}$ shape memory alloy with near-zero hysteresis, Script Mater. 103 (2015) 30–33, https://doi.org/10.1016/j.scriptamat.2015.02.030.
[52] H. Li, X.L. Meng, W. Cai, Shape memory behaviors in a $Ti_{50}Ni_{33.5}Cu_{12.5}Pd_4$ alloy with near-zero thermal hysteresis, J. Alloy. Compd. 765 (2018) 166–170, https://doi.org/10.1016/j.jallcom.2018.06.205.
[53] S. Miyazaki, Y. Igo, K. Otsuka, Effect of thermal cycling on the transformation temperatures of Ti-Ni alloys, Acta Metall. 34 (1986) 2045–2051, https://doi.org/10.1016/0001-6160(86)90263-4.